University of Reading

Observations of water transparency in China's lakes from space

Article

Accepted Version

Creative Commons: Attribution-Noncommercial-No Derivative Works 4.0

Liu, D., Duan, H., Loiselle, S., Hu, C., Zhang, G., Li, J., Yang, H. ORCID: https://orcid.org/0000-0001-9940-8273, Thompson, J. R., Cao, Z., Shen, M., Ma, R., Zhang, M. and Han, W. (2020) Observations of water transparency in China's lakes from space. International Journal of Applied Earth Observation and GeoInformation, 92. 102187. ISSN 0303-2434 doi: 10.1016/j.jag.2020.102187 Available at https://centaur.reading.ac.uk/95940/

It is advisable to refer to the publisher's version if you intend to cite from the work. See Guidance on citing.
Published version at: https://www.sciencedirect.com/science/article/pii/S0303243420304049
To link to this article DOI: http://dx.doi.org/10.1016/j.jag.2020.102187

Publisher: Elsevier

All outputs in CentAUR are protected by Intellectual Property Rights law, including copyright law. Copyright and IPR is retained by the creators or other copyright holders. Terms and conditions for use of this material are defined in the End User Agreement.

www.reading.ac.uk/centaur

University of Reading

CentAUR

Central Archive at the University of Reading

Reading's research outputs online

Observations of water transparency in China's lakes from space

Dong Liu[a], Hongtao Duan[a,b,*], Steven Loiselle[c], Chuanmin Hu[d], Guoqing Zhang[e], Junli Li[f], Hong Yang[g,i], Julian R. Thompson[h], Zhigang Cao[a], Ming Shen[a], Ronghua Ma[a], Min Zhang[i], Weixiao Han[j]

a Key Laboratory of Watershed Geographic Sciences, Nanjing Institute of Geography and Limnology, Chinese Academy of Sciences, Nanjing 210008, China
b College of Urban and Environmental Sciences, Northwest University, Xi'an, 710127, China
c Dipartimento Farmaco Chimico Tecnologico, CSGI, University of Siena, 53100 Siena, Italy
d College of Marine Science, University of South Florida, 140 Seventh Avenue, South, St. Petersburg, FL, 33701, USA
e Key Laboratory of Tibetan Environmental Changes and Land Surface Processes, Institute of Tibetan Plateau Research, Chinese Academy of Sciences, Beijing 100101, China
f Xinjiang Institute of Ecology and Geography, Chinese Academy of Sciences, Urumqi 830011, China
g Department of Geography and Environmental Science, University of Reading, Whiteknights, Reading, RG6 6AB, UK
h Department of Geography, University College London, London, WC1E 6BT, UK
i State Key Laboratory of Lake Science and Environment, Nanjing Institute of Geography and Limnology, Chinese Academy of Sciences, Nanjing 210008, China
j Key Laboratory of Remote Sensing of Gansu Province, Northwest Institute of Eco-Environment and Resources, Chinese Academy of Sciences, Lanzhou 730000, China

Abstract

Water transparency, usually denoted by Secchi disk depth (SSD), represents the first-order description of water quality and has important implications for the diversity and productivity of aquatic life. In China, lakes supply freshwater and ecosystem services to nearly a billion people. Therefore, real time monitoring of lake transparency is of great significance. Moreover, understanding how and why transparency varies in space and time in response to different driving forces is needed to understand, manage, and predict lake water quality. Based on the time-saving and low-cost Google Earth Engine cloud platform, this study developed a new algorithm for quickly mapping SDDs in Chinese lakes. SDDs were retrieved for 412 Chinese lakes (> 20 km^2) for the period 2000–2018. Results demonstrated that lake water depth spatially differentiated transparency. Deep lakes usually had high transparency and water depth explained 88.81 % of the spatial variations. With increasing catchment vegetation coverage and lake water depth, 70.15 % of lakes witnessed increasing transparency during 2000–2018. Of these 42.72 % were significant ($p<0.05$). Transparency of deep lakes was generally determined by phytoplankton density not sediment resuspension. Minimum transparency occurred in summer. Future increases in lake water levels in response to factors such as climate change may contribute to further improvements in transparency. Management should focus on controlling eutrophication and increasing vegetation cover in catchments.

1. Introduction

Lakes provide invaluable ecosystem services such as drinking water, spiritual/recreational places, and habitat that supports extensive biological diversity (Olmanson et al., 2008). With intensifying human activities and climate warming, however, many lakes have suffered from eutrophication (Wang et al., 2018), algal blooms (Ho et al., 2019), and transparency declines (McCullough et al., 2013). Water transparency, indicating the water depth where a Secchi disk or Secchi tube is no longer viewable, is one of the most intuitive, oldest, least expensive and easiest ways to evaluate water quality (Carlson, 1977; Lee et al., 2015; Tyler, 1968). Secchi disk depth (SDD) has been collected for nearly two centuries and regular measurement can reveal general trends in water quality (Feng et al., 2019; Lottig et al., 2014; McCullough et al., 2013; Olmanson et al., 2008).

SDD is largely determined by optically active particulate matter, namely total suspended matter (TSM) or phytoplankton denoted by chlorophyll-a (Chl-a) usually, and can be monitored using satellite data observed from space (Feng et al., 2019; Lee et al., 2015; McCullough et al., 2013; Olmanson et al., 2008). With the advantages of large-scale synchronous observation and long-term image archive, satellite remote sensing is an optimal choice to explore SDD variations in lakes at different spatio-temporal scales (Feng et al., 2019; McCullough et al., 2013; Olmanson et al., 2008). Generally, the traditional process for remotely monitoring SDD contains three steps. First, we need to download a large amount of satellite data from the source (Li et al., 2019; Shang et al., 2016), for example, the NASA ocean color site (https://oceancolor.gsfc.nasa.gov/). Second, we need to do the atmospheric correction using a professional software, the SeaWiFS data analysis system (SeaDAS) usually (IOCCG, 2018; Shi et al., 2018; Song et al., 2020). Then, a regional calibrated algorithm is applied to retrieve SDD from the corrected satellite data (McCullough et al., 2012; Olmanson et al., 2008). These laborious and professional work make it hard to quickly map SDDs, especially for scattered lakes in a national or global scale.

Since the 2010s, global users have access to the services offered by the Google Earth Engine (GEE) cloud platform (https://earthengine. google.com). The GEE cloud stores vast amounts of long-term archived satellite data and provides computational infrastructure plus online access to these data (https://code.earthengine.google.com/). Combining the available satellite images with petabyte processing power put real-time monitoring of earth's lakes within reach (Pekel et al., 2016). Based on three million Landsat images from the GEE, Pekel et al. (2016) mapped global surface waters in high-resolution and revealed their long-term changes. Recently, Ho et al. (2019) also mapped surface phytoplankton blooms in global lakes using the Landsat 5 Thematic Mapper images since the 1980s from the GEE cloud platform. To the best of our knowledge, however, quickly mapping lake transparency in a large area using the GEE cloud platform has not been reported.

China covers an area of 9.6 million square kilometers and has ~2700 lakes with a surface area greater than 1 km2 (Ma et al., 2010; Zhang et al., 2019). Since China's reform and opening-up in the 1980s, rapid economic development has exerted massive pressure on lake ecosystems and led to water quality deterioration (Duan et al., 2009; Huang et al., 2019; Tong et al., 2017). To improve lake environments, the Chinese government has implemented major strategies for alleviating general water pollution since 2000 (Huang et al., 2019; Qin et al., 2007; Tong et al., 2017). These efforts mainly aim to control nutrient pollution in eastern Chinese lakes and have effectively improved water quality (Huang et al., 2019; Qin et al., 2007; Zhou et al., 2017). However, the eastern zone only contains ~40 % of Chinese lakes (Ma et al., 2010) and lakes in the western Qinghai-Tibet Plateau (39 %) were barely considered (Huang et al., 2019; Tong et al., 2017; Zhou et al., 2017). To better manage and improve lake water quality, a nationwide assessment is urgently needed.

The present study developed a new algorithm for quickly mapping lake SDD using the satellite data available from the GEE cloud platform. Then, mean SDDs at different time scales (climatology, year, and month) during 2000–2018 of 412 Chinese lakes with a water area large than 20 km2 were remotely estimated. Based on the multi-source earth science data, spatio-temporal variations of SDDs in Chinese lakes were analyzed.

2. Materials and methods

2.1. The study area

China is the world's most populous country and the fourth largest in area. The digital elevation model (DEM) ranges from 0m in the east to 8790m in the west Qinghai-Tibet Plateau (Fig. 1). Annual mean air temperature is ~25 ℃ in the south but about -5 ℃in the north and the Qinghai-Tibet Plateau (Liu et al., 2020a). The annual total precipitation in the southeast China can reach up to ~3000mm but only ~10mm in the northwest (Liu et al., 2020a). Being influenced by the East Asian Monsoon, wind speed, air temperature, and precipitation vary seasonally (Song et al., 2020). Lakes in China are distributed from plain to plateau, encompass a wide range of biomes, and can be divided into five geographical zones (Ma et al., 2010; Wang and Dou, 1998): the Inner Mongolia-Xinjiang lake zone (IMXL), the Tibetan Plateau lake zone (TPL), the Yunnan-Guizhou plateau lake zone (YGPL), the northeast plain and mountain lake zone (NPML), and the eastern plain lake zone (EPL) (Fig. 1). Lakes in the east EPL and NPML are characteristically shallow compared to lakes in other three west zones (Wang and Dou, 1998).

2.2. In-situ data across China

During 2003–2018, 2236 in-situ SDDs were measured in 299 Chinese lakes (Fig. 1, Table 1). Of them, 148, 110, 126, 285, and 1567 were located within the IMXL, TPL, YGPL, NPML, and EPL, respectively (Fig. 1, Table 1). In each fieldwork episode, SDD was measured at the boat's shaded side using a 25-cm diameter Secchi disk by following the protocols proposed by NASA (Mueller et al., 2003). When measuring SDD, surface water within 0−30 cm water depth was collected using a standard 2-liter polyethylene water sampler. Back on shore, raw water was filtrated through Whatman GF/C™ (1.2-μm pore size, Φ47 mm) and Whatman GF/F (0.7-μm pore size, Φ47 mm) filters to obtain the Chl-a and TSM samples, respectively (Knap et al., 1994; Mueller et al., 2003). Note that TSM and Chl-a samples were not collected for all stations with SSD measurements.

In the laboratory, the Chl-a sample was soaked with 90 % ethanol in the dark for 24 h (Liu et al., 2019). Then, the extracting solution was heated to 80−90℃ for 3−5 min and measured via a Shimadzu UV2401 Spectrophotometer by following the JGOFS protocols (Knap et al., 1994). Finally, the Chl-a concentration was calculated using the measured light absorbance at 630, 645, 663, and 750 nm (Knap et al., 1994; Liu et al., 2020b). TSM concentration was determined gravimetrically by drying the TSM sample repeatedly (40℃ for 6 h) until the weight difference was less than 0.01 mg (Liu et al., 2019; Strickland and Parsons, 1972).

In addition to the above, monthly in-situ SDDs at 25 stations in Lake Taihu during 2000–2015 were also included in the current study. More details about the sampling locations can be found in Shi et al. (2018). These data were usually collected in the first half of each month and stored in the Land and Watershed Data Center (http://lake.geodata.cn/).

2.3. MODIS images in the GEE

In this study, the long-term archived remote sensing data during 2000–2018 recorded by the Moderate Resolution Imaging Spectroradiometer (MODIS) onboard the Terra satellite were adopted. With a daily revisiting period, the MODIS data have significant advantages in

monitoring highly dynamic lakes (Cao et al., 2017; Feng et al., 2019; McCullough et al., 2012). This study used the daily land surface reflectance product (MOD09GA) with a spatial resolution of 500m×500 m. The MOD09GA was calibrated for atmospheric conditions such as Rayleigh scattering, gasses, and aerosols. It provides spectral reflectance at seven bands with central wavelengths of 469, 555, 645, 859, 1240, 1640, and 2130 nm, which can be used for monitoring inland waters (Feng et al., 2018). The MOD09GA also contains a quality assurance band, which labels the cloud state, shadow, land/water, aerosol quantity, snow/ice, and others. All the MOD09GA products are available in the GEE cloud platform (https:// developers.google.com/earth-engine/datasets/catalog/MODIS_006_ MOD09GA).

2.4. Data on climate, geography, and human activities

Monthly mean wind speed over the lakes during 2000–2018 was sourced from the European Centre for Medium-Range Weather Forecasts (ECMWF, www.ecmwf.int). Using the monthly mean wind speed, annual climatological values were further calculated. Lake areas in 1990, 1995, 2000, 2005, 2010, and 2015 were from Zhang et al. (2019). The DEM from the Shuttle Radar Topography Mission (DEM/ SRTM) with a spatial resolution of 30m was sourced from NASA (earthdata.nasa.gov). Using the DEM/SRTM, mean lake depth was calculated by a geo-statistical method (Messager et al., 2016).

The lake catchment extents were identified using the WWF HydroBASINS tool provided by the USGS. To define the catchment extent, the HydroSheds dataset was processed with a user-friendly graphical interface (www.hydrosheds.org). We also checked the software output results manually. Then, using the lake catchment boundary data, the monthly mean land surface temperature during 2000–2018 was calculated from the monthly MODIS product MOD11A1; monthly mean normalized difference vegetation index (NDVI) was calculated from the monthly MODIS product MOD13A2. Both MOD11A1 and MOD13A2 were sourced from the USGS (https://lpdaac.usgs.gov/). Monthly total precipitation for each catchment was calculated from the monthly Tropical Rainfall Measuring Mission product TRMM3B43 (https://disc.gsfc.nasa.gov/). Using the monthly remote sensing products, climatological values of land surface temperature, NDVI, and precipitation were also computed. These calculations were proceed using the Matlab software 2012.

As in other studies (Liu et al., 2020b; Zhou et al., 2017), we used population density to indicate human activity intensity. To calculate mean population density in each studied lake catchment, we adopted the reprocessed grid-based population density data in 2010, the middle year of the studied period 2000–2018. The data were with a spatial resolution of 1000m×1000m (www.geodoi.ac.cn).

2.5. Statistical analysis and accuracy assessment

Correlation analyses were performed to indicate the direction (positive or negative) and strength (2-tailed significance test) of the linear relationships between SDD and various explanatory variables. Multiple general linear model (GLM) analyses were conducted to quantify the relative contributions of different impact factors (Feng et al., 2019; Tao et al., 2015). Based on the information-theoretic approach and Akaike information criteria (Burnham and Anderson, 2002), the multiple GLM analysis can reduce model selection bias (Tao et al., 2015). All these statistical analyses were conducted in the SPSS 18 (IBM SPSS, Chicago, IL).

Referring to Cao et al. (2018), the mean absolute percent difference (MAPD), root mean square error (RMSE), and bias were adopted to assess the modeling results. They are defined as Eq. (1).

$$\mathrm{MAPD}=\left\{\sum\left|\frac{[X_i^{\mathrm{mod}eled}-X_i^{in-situ}]}{x_i^{in-situ}}\right|\right\}\times 100/N$$
$$\mathrm{RMSE}=\left\{\frac{\sum[X_i^{\mathrm{mod}eled}-X_i^{in-situ}]^2}{N}\right\}^{1/2}$$
$$\mathrm{bias}=\left\{\frac{1/N\times\sum[X_i^{\mathrm{mod}eled}-X_i^{in-situ}]}{mean(X_i^{in-situ})}\right\}\times 100 \quad (1)$$

where $X_i^{in-situ}$ and $X_i^{modeled}$ are the in-situ and modeled SDDs, respectively. N denotes the total number of samples.

3. The algorithm for quickly mapping SDD using GEE

Using the in-situ SDDs (Section 2.2), we developed a remote sensing algorithm applicable to the MOD09GA dataset. For each in-situ SDD, synchronous cloud-free water reflectance within a time window of± 3 h was found by following the match-up criteria used by NASA (Bailey and Werdell, 2006). For the in-situ SDD higher than 200 cm, if no valid water reflectance was found, we expanded the time window from one to seven days in order. Kloiber et al. (2002) reported that increasing the time window between in-situ SDD and image collection within±7 days could yield reasonable results. 38 new match-ups were found by relaxing the time window. Moreover, the matched pairs within two pixels to the shore were removed to avoid the land adjacency effects (Feng and Hu, 2017). Finally, valid match-ups were found for 489 in-situ SDDs in 128 lakes (Fig. 1). Of them, 366 (75 %) were selected randomly as the training dataset and the remaining 123 (25 %) were taken as the testing dataset.

For lakes in the EPL with low SDDs, water reflectance of MODIS at the red band (R645) was usually adopted for remotely retrieving SDD or TSM (Feng et al., 2019; Li et al., 2019; Shi et al., 2018). To remotely monitor lakes in the TPL with high SDDs, however, Liu et al. (2017) used the water reflectance of MODIS at the green band (R555). Based on previous studies, therefore, we adopted both R645 and R555 to develop an algorithm for remotely retrieving SDDs in all Chinese lakes. For the training dataset, we tested various band combinations (ratio, difference) and evaluated their relations (linear, exponential, power, and polynomial) to in-situ SDDs. When using the mean values of R645 and R555, the power function was satisfactory, with R^2=0.83 (Fig. 2a). The power function underestimated the SDDs in clear lakes, so we used a piecewise function to improve the algorithm performance (Fig. 2a). For lakes with high SDDs and low water reflectance, an exponential formula was used (Eq. (2), Fig. 2a). We tested the results when moving the intermediate variable R from 0 to 0.08 with an interval of 0.001 and achieved the best model performance when R=0.016. Therefore, for lake water with $R \leq 0.016$, an exponential formula was used to remotely estimate SDD (Eq. (2), Fig. 2a). On the contrary, for lake water with R>0.016, a power function was applied to estimate SDD (Eq. (2), Fig. 2a).

$$\mathrm{SDD}=1699.72\times e^{-170.92\times R}, R\leq 0.016$$
$$\mathrm{SDD}=0.36\times R^{-1.39}, R>0.016$$
$$R=(R555+R645)/2\pi \quad (2)$$

where *R*555 and *R*645 are surface reflectance of MOD09GA at the green and red bands, respectively. By dividing the constant π, the surface reflectance is converted to water-leaving

reflectance by ignoring the bidirectional effects (Wang et al., 2018). Moreover, the relaxed time window only increased match-ups with low water reflectance and did not show significant impacts on the model performance (Fig. S1).

The two nearshore pixels were excluded, so only lakes with an area larger than 6.25 km^2 can be monitored by the MODIS data with a spatial resolution of 500 m. However, most lakes are irregularly shaped. To ensure enough valid MODIS pixels left, we set the area threshold as 20 km2. Based on the GEE cloud platform, the Eq. (2) was applied to daily MOD09GA during 2000–2018 to remotely estimate SDDs in large Chinese lakes (> 20 km2). The QA band of MOD09GA was first used to mask out the land, cloud, cloud shadow, and snow/ice. Then, an OTSU algorithm was further applied on the normalized difference water index so as to remove the impacts of sun glint and aquatic vegetation. For a specific pixel, we obtained the monthly and annual mean SDDs by averaging all valid daily results. Then, the lake-based mean SDDs were further calculated. In the calculation, only ice-free results during May-September were used for the IMXL, TPL, and NPML (Cai et al., 2019). Moreover, lakes with valid SDDs in less than 10 years were not considered. Finally, 412 lakes were left to investigate the spatio-temporal variations of SDD and possible driving forces.

4. Results and discussion

4.1. The algorithm validation

The newly developed algorithm was validated using the in-situ SDDs (Section 2.2). Eq. (2) was calibrated using the training dataset (N=366), for which the MAPD, RMSE, and bias were 32.42 %, 53.65 cm, and -26.47 %, respectively (Fig. 2b). The testing dataset (N=123) was used to evaluate the developed algorithm (Eq. (2)). The MAPD, RMSE, and bias were 32.72 %, 48.91 cm, and -27.32 %, respectively (Fig. 2b). For China' third largest freshwater lake (Lake Taihu in the EPL), annual mean SDD was calculated using the monthly in-situ data during 2000–2015 (Section 2.2) and compared with the satellite derived results. The MAPD, RMSE, and bias were 10.58 %, 5.74 cm, and 4.55 %, respectively (Fig. S2a). The satellite-derived annual mean SDD was also significantly linearly related to the measured results, with Pearson's $r = 0.53$ and $p < 0.05$ (Fig. S2a).

The new algorithm was also compared with three previously reported algorithms developed for the MODIS data (Feng et al., 2019; Lee et al., 2015; Li et al., 2019; Liu et al., 2017).

1) Lee et al. (2015) proposed a mechanistic model relying on the diffuse attenuation coefficient at a wavelength with the maximum transparency to remotely estimate SDD. The synthesized dataset published by the IOCCG contains water reflectance, from which we estimated SDDs using the algorithms developed by Eq. (2) and Lee et al. (2015). The results showed that the MAPD, RMSE, and bias were 59.32 %, 1021.37 cm, and 28.14 %, respectively (Fig. 2c). Eq.

(2) overestimates SDDs of highly clear waters (SDD > 2000 cm), leading to the high uncertainty in the differences (Fig. 2c). This was because Eq.(2) was calibrated using SDDs of 1.3–1650 cm for Chinese lakes (Table 1), but the IOCCG dataset covered a wide SDD range of 101.01–4246.51 cm. Using the algorithm of Lee at al. (2015), Feng et al. (2019) investigated the spatio-temporal variations of SDDs for lakes in the EPL. Comparing our modeled climatological mean SDDs during 2000–2018 in different lakes with their results, we obtained MAPD, RMSE, and bias of 35.68 %, 66.8 cm, and -35.13 %, respectively (Fig. 2c).

2) For lakes in the TPL, Liu et al. (2017) used only the water reflectance at the green band of MODIS (R555) to remotely retrieve SDD. For the 267 studied lakes in the TPL, the satellite-derived climatological mean SDDs during 2000–2018 by this study were compared with

those from their algorithms. The MAPD, RMSE, and bias were 15.36 %, 31.98 cm, and -0.01 %, respectively (Fig. 2d).

3) For the fourth largest China's freshwater lake (Lake Hongze), Li et al. (2019) derived annual mean SDDs from 2003 to 2017 using the MODIS data, as shown in Fig. S2b. Although the modeled annual mean SDDs by this study were lower than those by Li et al. (2019), probably due to our exclusion of the pixels adjacent to land with high SDDs (Section 3), they were significantly linearly correlated (N=15; $R2=0.39$; $p < 0.05$). The MAPD, RMSE, and bias were 27.44 %, 14.39 cm, and -27.24 %, respectively (Fig. S2b).

In summary, the satellite-derived SDDs from this study were comparable to those reported previously. Therefore, the newly developed algorithm could be applied to MOD09GA to remotely estimate SDDs in Chinese lakes.

4.2. Impacts of water depth on the spatial variations

Satellite-derived climatological SDD during 2000–2018 was used to represent its spatial distribution in different lakes across China. Although SDD varied spatially within a specific lake zone, high transparent lakes were generally located in the southwest plateau regions (Fig. 3a). During 2000–2018, the IMXL, TPL, YGPL, NPML, and EPL had mean SDDs of 139.7 ± 193.96, 182.41 ± 184.29, 404.63 ± 363.98, 55.05 ± 33.46, and 92.9 ± 90.09 cm, respectively (Fig. 3b). On the whole, mean SSD in the three west mountainous lake zones (180.28 ± 171.29 cm) was double that in the two east plain zones (78.01 ± 40.54 cm). As shown in Fig. 3b, the highest mean SDD was found for the YGPL (404.63 ± 363.98 cm), and the lowest for the NPML (55.05 ± 33.46 cm). 72 of the 313 lakes in the three western zones were also characterized by low transparency, with mean SDDs below 50 cm (Fig. 3a). For the TPL, most lakes with low SDDs were located in the northwest with limited in-situ values (Figs. 1, 3a), which caused the obvious difference between the modeled and in-situ SDDs. (Fig. 3b).

Lake SDD is co-determined by various environment variables in the lake and catchment (Feng et al., 2019). For Chinese lakes, in-situ data showed that SDD was significantly related to TSM ($R2=0.84$, $p < 0.001$, N=1792). TSM in the lake comes from three main sources: phytoplankton growth, sediment resuspension, and riverine input. For phytoplankton growth, temperature has an important influence (Rhee and Gotham, 1981) and was significantly negatively related to SDD (Fig. S3b, Table S1). For in-lake sediment resuspension, the wind is a key driver (Webster and Hutchinson, 1994; Xue et al., 2015) and water depth is a moderator (Carper and Bachmann, 1984). Both wind speed and water depth showed significant relationships to SDD (Figs. S3a, 3c, Table S1). Riverine inputted TSM are influenced by terrestrial soil erosion, controlled by basin precipitation, vegetation coverage (NDVI), and basin slope (Boardman and Favis-Mortlock, 1998; Wang et al., 2015, 2019; Yue et al., 2016). Human activities (population density) also impact TSM content via some means including increasing available nutrients for phytoplankton growth (Liu et al., 2020b; Wang et al., 2018), changing land cover which in turn impacts soil erosion (Wang et al., 2015), and mining sand which increases sediment resuspension (Cao et al., 2017).

For Chinese lakes, the multiple GLM results showed that the spatial distribution of SDD was mainly influenced by water depth and wind speed (Fig. 3d). Lake water depth spatially correlated well with SDD. Considering all studied lakes (N=412), satellite-derived mean SDD was significantly linearly related to water depth, with $R2=0.49$ and $p < 0.01$ (Fig. 3c). Except for the NPML, significant linear relationships between SDD and water depth were also observed for the other four zones, respectively. As a whole, water depth explained 88.81 % of the spatial variations of SDDs in Chinese lakes (Fig. 3d). For the IMXL, TPL,

YGPL, and EPL, its contributions were 72.91 %, 90.05 %, 44.36 %, and 35.47 %, respectively (Fig. 3d). It's worth noting that wind speed also accounted for 36 % of the spatial variations of SDDs in shallow lakes in the EPL (Figs. 3d, S3a).

4.3. Increasing transparency and catchment greening

Generally, Chinese lakes had become more transparent over the past two decades. The overall trend was characterized by an annual mean increase of SDD by 2.77 ± 6.12 cm/yr (Fig. 4). Of the studied 412 lakes, 70.15 % witnessed increasing SDDs during 2000–2018 and 42.72 % increased significantly ($p < 0.05$) (Fig. 4). Increase rates for the western lakes were high (Fig. 4), with mean values varying from the IMXL (3.56 ± 4.45 cm/yr), through the TPL (6.16 ± 6.42 cm/yr), to the YGPL (8.74 ± 7.67 cm/yr). Many eastern lakes also showed significant increasing SDDs, but with lower change rates of 1.98 ± 1.6 cm/yr and 0.99 ± 1.4 cm/yr for the EPL and NPML, respectively (Fig. 4). Other studies also reported that eastern Chinese lakes had improved water quality indicated by nutrient concentration (Tong et al., 2017; Zhou et al., 2017). For the EPL, Feng et al. (2019) reported that many lakes showed increasing SDDs during 2003−2016. The other 29.85 % lakes showed decreasing SDDs with a mean change rate of only -2.36 ± 2.58 cm/yr, and 10.44 % presented significantly (Fig. 4).

Watershed vegetation coverage indicated by NDVI had important impacts on SDD changes during 2000–2018. Over the past decades, the Chinese government had launched some large-scale vegetation rehabilitation projects, for example, the "Grain-for-Green Program" since 1999 (Ostwald et al., 2011; Wang et al., 2015). These projects covered all Chinese provinces (www.stats.gov.cn) and increased afforestation area of 109.23×104 km2 during 2000–2018 (Fig. S4a). As a result, NDVI increased in 382 lake catchments (92.72 %), with 277 significantly (Figs. S4d, S5c). The multiple GLM results showed that increasing NDVI explained much of the significant SDD increases: 44.95 %, 37.87 %, 75.66 %, 58.12 %, and 36.34 % for lakes in the IMXL, TPL, YGPL, NPML, and EPL, respectively (Table 2). For significant SDD decreases in the IMXL, TPL, NPML, and EPL, NDVI also explained 12.11 %, 29.62 %, 24.5 %, and 30.45 %, respectively (Table 2).

Climate change also showed apparent influences on SDD variations during 2000–2018, but differed regionally (Table 2). Climate change led to regional differences for changes in wind speed, temperature, and precipitation (Figs. S4b, S5a, Table S3). Increased wind speed happened to most lakes in the western zones (Fig. S5a). Increasing wind speed explained 68.96 % and 21.80 % of SDD decreases in the IMXL and EPML, respectively (Table 2). Increased temperature was observed for many lakes in the TPL and EPL (Fig. S5b). Increasing temperature melted glaciers, raised lake water levels (Qiao et al., 2019; Zhang et al., 2019), and contributed 24.98 % of SDD increases in the TPL (Table 2). On the contrary, increasing temperature explained 23.65 % of SDD decreases in the EPL (Table 2). Increased precipitation happened to most studied lakes (Fig. S5d). For lakes in the EPL, increasing precipitation explained 27.81 % and 22.46 % of SDD increases and decreases, respectively (Table 2). It also explained 21.88 % of SDD decreases in the NPML (Table 2).

4.4. Opposite seasonal cycles between west and east

Using the monthly climatological SDD values of each studied lake, we manually identified the seasonal variability cycle of SDD. The results showed two general, but opposite, seasonal behaviors (Figs. 5,6). Type T1 showed a "triangular shape" with a maximum SDD in summer (June-August); in contrast, type T2 had an "inverted triangle shape" with a minimum SDD in summer (Fig. 6). More specifically, only ice free data during May-September were used for the three western zones. As a result, type T1 contained three subclasses (T11, T12 and T13) and type T2 included two subclasses (T21 and T22) (Fig. 6). For all studied lakes, there were

77 (18.69 %), 108 (26.21 %), 166 (40.29 %), 11 (2.67 %), and 50 (12.14 %) of the types T11, T12, T13, T21, T22, respectively (Fig. 5). For lakes in the TPL, 78 (42.39 %), 140 (76.09 %), and 44 (23.91 %) were in the types T12, T13, T22, respectively (Fig. 5f). Overall, 85.19 % of the studied lakes were in the type T1 (Fig. 6).

All studied lakes in the EPL were identified as type T1 (Fig. 6). This seasonal cycle was reported previously in some case studies (Feng et al., 2012, 2019; Shi et al., 2018). Feng et al. (2019) had reported that many lakes in the EPL had peaked SDDs in summer. Lakes in the EPL had a mean water depth of only 3.42m (Table S3) and their SDDs were controlled by sediment resuspension (Feng et al., 2019; Zhang et al., 2006).

Relationships between in-situ data proved the influence of inlake sediment resuspension. As shown in Fig. S6a-b, in-situ SDD was highly related to TSM ($R2=0.79$, $p < 0.001$) but lowly correlated with Chl-a ($R2=0.09$, $p < 0.001$). Wind speed in summer was weaker than that in winter (Fig. S7a). Moreover, precipitation in summer was significantly higher than that in winter (Fig. S7d). Abundant precipitation in summer raised lake water levels. For the three largest lakes, the Dongting, Poyang, and Chaohu, in-situ water levels were apparently higher in summer (Feng et al., 2019). Low wind speed and high water level led to weak sediment resuspension and high SDD in summer. For the Dongting and Poyang lakes, the stable lake flow conditions also contributed to the high SDDs in summer (Feng et al., 2012).

All studied lakes in the YGPL belonged to type T2 (Fig. 6). These lakes were characterised by deep water with a mean depth of 27.09 m, high catchment vegetation coverage, and low soil erosion (Fig. S8, Table S3). The strong precipitation in summer (Fig. S7d) could not significantly elevate water depth for these deep lakes. Their SDDs were determined by algal production and seasonally changed following phytoplankton abundance. In-situ data showed that SDD was negatively correlated with Chl-a ($R2=0.78$, $p < 0.01$) and TSM was positively related to Chl-a ($R2=0.82$, $p < 0.01$) (Fig. S6c-d). High temperature was favorable for phytoplankton growth (Rhee and Gotham, 1981) and caused low SDDs in summer (Fig. S7e).

Lakes in the other three zones (IMXL, TPL, NPML) had a mixed distribution of types T1 and T2 (Fig. 6). For Lake Hulun in the NPML, Song et al. (2017a) reported that the light attenuation of photosynthetically active radiation, negatively related to SDD, had a minimum value in summer (July-August), which was consistent with our SDD result (Fig. 6). The same as lakes in the EPL, lakes in types T12 and T13 were usually shallow with a mean depth of 8.05m and turbid with a mean SDD of 154.99 cm. Their SDDs were also majorly influenced by sediment resuspension. For in-situ data with SDDs<100 cm, SDD was also significantly related to TSM ($R2=0.71$, $p < 0.01$), but not to Chl-a (Fig. S6e). Interestingly, the month with maximum SDD was spatially different (Fig. 6) and roughly followed the movement of the summer strong rainfall staying in the EPL from mid-June to mid- July and gradually moving north to NPML from July to August (Chen et al., 2004; Chiang et al., 2017). On the contrary, as for lakes in the YGPL, type T22 lakes were relatively deep with a mean depth of 17.24m and limpid with a mean SDD of 219.66 cm. Their SDDs were also notably impacted by phytoplankton production. For in-situ data with SDDs>100 cm, SDD was also significantly related to both TSM and Chl-a, with $p < 0.01$ (Fig. S6f).

Our data clearly showed the different seasonal patterns of SDDs in Chinese lakes, while only ice-free months during May-September were considered for the IMXL, TPL, and NPML zones (Fig. 6). In fact, lake ice phenology varied for different lakes even in the same zone (Cai et al., 2019). For different lakes, therefore, taking all ice-free months into consideration could improve our understanding of seasonal patterns of SDDs in Chinese lakes.

4.5. Theoretical explanations for spatio-temporal variability of SDD

Theoretically, SDD is co-determined by three optically active components: colored dissolved organic matter (CDOM), Chl-a, and nonalgal particle (IOCCG, 2018). The latter two can be collectively referred to as TSM. For the large Chinese lakes (> 20 km2), SDDs were determined by TSM. First, in-situ SDD was significantly related to TSM, with R2=0.84 and $p < 0.001$ (N=1792). Moreover, previous studies reported that high CDOM was limited to small closed saline lakes in China (Song et al., 2017b). Third, light absorption by CDOM exponentially decreases with increasing wavelength, so its impacts on the developed algorithm using the green and red bands (Section 3) were considered as negligible. TSM had three main sources: sediment resuspension, autochthonous phytoplankton production, and allochthonous riverine input (Fig. 7).

In-lake sediment resuspension followed the lake sedimentology principles impacted by wind and water depth (Håkanson and Jansson, 1983). Wind can drive sediment resuspension (Fig. 7). This explained the wind's effects on the spatial distribution of SDDs in the NPML (Fig. 3d) and decreasing SDDs in the IMXL during 2000–2018 (Table 2). On the contrary, increasing water depth can weaken sediment resuspension (Fig. 7). TSM was mainly composed of suspended sediment (Fig. S6), so water depth had important impacts on the spatial distribution of SDDs in Chinese lakes (Fig. 3d). Precipitation also increased SDD during 2000–2018 by elevating the water level and vice versa (Table 2). What is more, the maximum SDD in summer differed spatially (Fig. 6) and followed the strong precipitation movement (Chen et al., 2004; Chiang et al., 2017). Increasing temperature in the TPL also increased SDD (Table 2, Fig. S5b) by elevating water level through melting glaciers (Qiao et al., 2019; Zhang et al., 2019).

Autochthonous phytoplankton production followed the phenology principle. Temperature increase is favorable for phytoplankton growth (Edwards and Richardson, 2004; Rhee and Gotham, 1981). For lakes in the YGPL, SDDs were determined by phytoplankton density (Fig. S6c- d). In these cases, temperature explained 29.47 % of the spatial distribution of SDDs in the YGPL (Fig. 3d). High temperature also promotes algal proliferation (Edwards and Richardson, 2004; Rhee and Gotham, 1981) and caused minimum SDDs for type T2 lakes in summer (Fig. 6).

Allochthonous riverine TSM input followed the soil erosion principle codetermined by precipitation and vegetation coverage in lake catchment (Meester, 1987). Precipitation can transport terrigenous soil particles into the lake and decrease SDD. This was obvious for the NPML and EPL with high precipitation (Fig. S8c). On the contrary, vegetation coverage can reduce soil erosion with a consequent decline in riverine TSM input (Wang et al., 2015; Yue et al., 2016). This was observed for its significant effects on increasing SDDs during 2000–2018 (Table 2).

5. Conclusions

In summary, this study developed a new algorithm that was used to rapidly map SDDs in large Chinese lakes (> 20 km2) from the MOD09GA data through the GEE cloud platform.

Water depth was a key impact factor on the spatio-temporal variability of transparency in Chinese lakes. First, overall, it explained 88.81 % of the spatial variations of SDDs. Second, during 2000–2018, increasing water depth increased SDD by weakening sediment resuspension, especially for lakes in the TPL. Third, water depth also influenced the seasonal variability cycle of SDD by changing the TSM (phytoplankton and suspended sediment) compositions. Future changes in lake levels in response to the processes described in this study may contribute to further increases in transparency. Management responses should focus on controlling lake eutrophication, a widely adopted strategy. Moreover, along with the long-term ecological restoration projects in China, improved vegetation coverage in catchments also had positive effects on increasing lake transparency.

CRediT authorship contribution statement

Dong Liu: Methodology, Writing - original draft, Visualization. Hongtao Duan: Conceptualization, Resources, Supervision. Steven Loiselle: Writing - review & editing. Chuanmin Hu: Writing - review & editing. Guoqing Zhang: Writing - review & editing. Junli Li: Writing - review & editing. Hong Yang: Writing - review & editing. Julian R. Thompson: Writing - review & editing. Zhigang Cao: Investigation. Ming Shen: Investigation. Ronghua Ma: Investigation. Min Zhang: Investigation. Weixiao Han: Investigation.

Declaration of Competing Interest

The authors declare that they have no known competing financial interests or personal relationships that could have appeared to influence the work reported in this paper.

Acknowledgments

We thank the Google Earth Engine for providing MODIS and other environment variable data (https://developers.google.com/earthengine/ datasets/). We also acknowledge the project titled “Lake water quality, quantity and biological resources investigation in China” for providing part of the dataset. This study was supported by the National Natural Science Foundation of China (Grants #41901299, #41971309, #41671358, #41431176, and #41771366), the Strategic Priority Research Program of the Chinese Academy of Sciences (Grant #XDA19040500), the Natural Science Foundation of Jiangsu Province (Grant #BK20181102), the Second Tibetan Plateau Scientific Expedition and Research Program (Grant #2019QZKK0202), and the Open Fund of State Key Laboratory of Lake Science and Environment, Chinese Academy of Sciences (Grant #2018SKL006).

References

Bailey, S.W., Werdell, P.J., 2006. A multi-sensor approach for the on-orbit validation of ocean color satellite data products. Remote Sens. Environ. 102, 12–23.

Boardman, J., Favis-Mortlock, D., 1998. Modelling Soil Erosion by Water. Springer.

Burnham, K.P., Anderson, D.R., 2002. Model-Selection and Multi-Model Inference: A Practical Information-Theoretic Approach. Springer.

Cai, Y., Ke, C.Q., Li, X., Zhang, G., Duan, Z., Lee, H., 2019. Variations of lake ice phenology on the Tibetan Plateau from 2001 to 2017 based on MODIS data. J. Geophys. Res. Atmos. 124, 825–843.

Cao, Z., Duan, H., Feng, L., Ma, R., Xue, K., 2017. Climate- and human-induced changes in suspended particulate matter over Lake Hongze on short and long timescales. Remote Sens. Environ. 192, 98–113.

Cao, F., Tzortziou, M., Hu, C., Mannino, A., Fichot, C.G., Del Vecchio, R., Najjar, R.G., Novak, M., 2018. Remote sensing retrievals of colored dissolved organic matter and dissolved organic carbon dynamics in North American estuaries and their margins. Remote Sens. Environ. 205, 151–165.

Carlson, R.E., 1977. A trophic state index for lakes. Limnol. Oceanogr. 22, 361–369. Carper, G.L., Bachmann, R.W., 1984. Wind resuspension of sediments in a prairie lake. Can. J. Fish. Aquat. Sci. 41, 1763–1767.

Chen, T.C., Wang, S.Y., Huang, W.R., Yen, M.C., 2004. Variation of the east asian summer monsoon rainfall. J. Clim. 17, 744–762.

Chiang, J.C.H., Swenson, L.M., Kong, W., 2017. Role of seasonal transitions and the westerlies in the interannual variability of the East Asian summer monsoon precipitation. Geophys. Res. Lett. 44, 3788–3795.

Duan, H., Ma, R., Zhang, Y., Zhang, B., 2009. Remote-sensing assessment of regional inland lake water clarity in northeast China. Limnology 10, 135–141.

Edwards, M., Richardson, A., 2004. Impact of climate change on marine pelagic phenology and trophic mismatch. Nature 430, 881–884.

Feng, L., Hu, C., 2017. Land adjacency effects on MODIS aqua top-of-atmosphere radiance in the shortwave infrared: statistical assessment and correction. J. Geophys. Res. Oceans 122, 4802–4818.

Feng, L., Hu, C., Chen, X., Tian, L., Chen, L., 2012. Human induced turbidity changes in Poyang Lake between 2000 and 2010: observations from MODIS. J. Geophys. Res. 117.

Feng, L., Hu, C., Li, J., 2018. Can MODIS land reflectance products be used for estuarine and inland waters. Water Resour. Res. 54, 3583–3601.

Feng, L., Hou, X., Zheng, Y., 2019. Monitoring and understanding the water transparency changes of fifty large lakes on the Yangtze Plain based on long-term MODIS observations. Remote Sens. Environ. 221, 675–686.

Håkanson, L., Jansson, M., 1983. Principles of Lake Sedimentology. Springer-verlag, Berlin.

Ho, J.C., Michalak, A.M., Pahlevan, N., 2019. Widespread global increase in intense lake phytoplankton blooms since the 1980s. Nature 574, 667–670.

Huang, J., Zhang, Y., Arhonditsis, G.B., Gao, J., Chen, Q., Wu, N., Dong, F., Shi, W., 2019. How successful are the restoration efforts of China's lakes and reservoirs? Environ. Int. 123, 96–103.

IOCCG, 2018. Earth observations in support of global water quality monitoring. In: Greb, S., Dekker, A., Binding, C. (Eds.), IOCCG Report Series, No. 17. International Ocean Colour Coordinating Group, Dartmouth, Canada.

Kloiber, S.M., Brezonik, P.L., Olmanson, L.G., Bauer, M.E., 2002. A procedure for regional lake water clarity assessment using Landsat multispectral data. Remote Sens. Environ. 82, 38–47.

Knap, A.H., Michaels, A., Close, A.R., Ducklow, H., Dickson, A.G., 1994. Protocols for the Joint Global Ocean Flux Study (JGOFS) Core Measurements; IOC Manuals and Guides No. 29. United National. Educational, Scientific and Cultural Organization (UNESCO), Paris, France.

Lee, Z., Shang, S., Hu, C., Du, K., Weidemann, A., Hou, W., Lin, J., Lin, G., 2015. Secchi disk depth: a new theory and mechanistic model for underwater visibility. Remote Sens. Environ. 169, 139–149.

Li, N., Shi, K., Zhang, Y., Gong, Z., Peng, K., Zhang, Y., Zha, Y., 2019. Decline in transparency of Lake Hongze from long-term MODIS observations: possible causes and potential significance. Remote Sens. 11, 177.

Liu, C., Zhu, L., Wang, J., Qiao, B., Ju, J., Huang, L., 2017. Remote sensing-based estimation of lake water clarity on the Tibetan Plateau. Prog. Geogr. 36, 597–609.

Liu, D., Duan, H., Yu, S., Shen, M., Xue, K., 2019. Human-induced eutrophication dominates the bio-optical compositions of suspended particles in shallow lakes: implications for remote sensing. Sci. Total Environ. 667, 112–123.

Liu, D., Bai, Y., He, X., Chen, C.A., Huang, T.H., Pan, D., Chen, X., Wang, D., Zhang, L., 2020a. Changes in riverine organic carbon input to the ocean from mainland China over the past 60years. Environ. Int. 134, 105258.

Liu, D., Du, Y., Yu, S., Luo, J., Duan, H., 2020b. Human activities determine quantity and composition of dissolved organic matter in lakes along the Yangtze River. Water Res. 168, 115132.

Lottig, N.R., Wagner, T., Norton Henry, E., Spence Cheruvelil, K., Webster, K.E., Downing, J.A., Stow, C.A., 2014. Long-term citizen-collected data reveal geographical patterns and temporal trends in lake water clarity. PLoS One 9, e95769.

Ma, R., Duan, H., Hu, C., Feng, X., Li, A., Ju, W., Jiang, J., Yang, G., 2010. A half-century of changes in China's lakes: global warming or human influence? Geophys. Res. Lett. 37.

McCullough, I.M., Loftin, C.S., Sader, S.A., 2012. High-frequency remote monitoring of large lakes with MODIS 500m imagery. Remote Sens. Environ. 124, 234–241.

McCullough, I.M., Loftin, C.S., Sader, S.A., 2013. Landsat imagery reveals declining clarity of Maine's lakes during 1995–2010. Freshw. Sci. 32, 741–752.

Meester, Td., 1987. Soil erosion and conservation. Earth. Rev. 24, 68–69. Messager, M.L., Lehner, B., Grill, G., Nedeva, I., Schmitt, O., 2016. Estimating the volume and age of water stored in global lakes using a geo-statistical approach. Nat. Commun. 7, 13603.

Mueller, J.L., Fargion, G.S., McClain, C.R., 2003. Ocean optics protocols for satellite ocean color sensor validation. Revision 4, Volume VI: Special Topics in Ocean Optics Protocols and Appendices. NASA/TM-2003-211621/Rev4.

Olmanson, L.G., Bauer, M.E., Brezonik, P.L., 2008. A 20-year Landsat water clarity census of Minnesota's 10,000 lakes. Remote Sens. Environ. 112, 4086–4097.

Ostwald, M., Moberg, J., Persson, M., Xu, J., 2011. The Chinese grain for green program - assessing the sequestered carbon from the land reform. In: World Renewable Energy Congress. Sweden.

Pekel, J.F., Cottam, A., Gorelick, N., Belward, A.S., 2016. High-resolution mapping of global surface water and its long-term changes. Nature 540, 418–422.

Qiao, B., Zhu, L., Yang, R., 2019. Temporal-spatial differences in lake water storage changes and their links to climate change throughout the Tibetan Plateau. Remote Sens. Environ. 222, 232–243.

Qin, B., Liu, Z., Havens, K., 2007. Eutrophication of Shallow Lakes With Special Referenc to Lake Taihu. Springer, China.

Rhee, G.-Y., Gotham, I.J., 1981. The effect of environmental factors on phytoplankton growth: temperature and the interactions of temperature with nutrient limitation. Limnol. Oceanogr. 26, 635–648.

Shang, S., Lee, Z., Shi, L., Lin, G., Wei, G., Li, X., 2016. Changes in water clarity of the Bohai Sea: observations from MODIS. Remote Sens. Environ. 186, 22–31.

Shi, K., Zhang, Y., Zhu, G., Qin, B., Pan, D., 2018. Deteriorating water clarity in shallow waters: evidence from long term MODIS and in-situ observations. Int. J. Appl. Earth Obs. Geoinf. 68, 287–297.

Song, K., Ma, J., Wen, Z., Fang, C., Shang, Y., Zhao, Y., Wang, M., Du, J., 2017a. Remote estimation of Kd(PAR) using MODIS and Landsat imagery for turbid inland waters in Northeast China. ISPRS J. Photogramm. Remote. Sens. 123, 159–172.

Song, K., Zhao, Y., Wen, Z., Fang, C., Shang, Y., 2017b. A systematic examination of the relationships between CDOM and DOC in inland waters in China. Hydrol. Earth Syst. Sci. 21, 5127–5141.

Song, K., Liu, G., Wang, Q., Wen, Z., Lyu, L., Du, Y., Sha, L., Fang, C., 2020. Quantification of lake clarity in China using Landsat OLI imagery data. Remote Sens. Environ. 243, 111800.

Strickland, J.D.H., Parsons, T.R., 1972. A practical handbook of seawater analysis. Bulletin 167. Tao, S., Fang, J., Zhao, X., Zhao, S., Shen, H., Hu, H., Tang, Z., Wang, Z., Guo, Q., 2015. Rapid loss of lakes on the Mongolian Plateau. Proc. Natl. Acad. Sci. U. S. A. 112, 2281–2286.

Tong, Y., Zhang, W., Wang, X., Couture, R.-M., Larssen, T., Zhao, Y., Li, J., Liang, H., Liu, X., Bu, X., He, W., Zhang, Q., Lin, Y., 2017. Decline in Chinese lake phosphorus concentration accompanied by shift in sources since 2006. Nat. Geosci. 10, 507–511.

Tyler, J.E., 1968. The secchi disc. Limnol. Oceanogr. 13, 1–6.

Wang, S.M., Dou, H.S., 1998. Chinese Lake Catalogue. Science Press, Beijing, China.

Wang, S., Fu, B., Piao, S., Lü, Y., Ciais, P., Feng, X., Wang, Y., 2015. Reduced sediment transport in the Yellow River due to anthropogenic changes. Nat. Geosci. 9, 38–41.

Wang, S., Li, J., Zhang, B., Spyrakos, E., Tyler, A.N., Shen, Q., Zhang, F., Kuster, T., Lehmann, M.K., Wu, Y., Peng, D., 2018. Trophic state assessment of global inland waters using a MODIS-derived Forel-Ule index. Remote Sens. Environ. 217, 444–460.

Wang, X., Quine, T.A., Zhang, H., Tian, G., Yuan, W., 2019. Redistribution of soil organic carbon induced by soil erosion in the nine river basins of China. J. Geophys. Res. Biogeosci. 124, 1018–1031.

Webster, I.T., Hutchinson, P.A., 1994. Effect of wind on the distribution of phytoplankton cells in lakes revisited. Limnol. Oceanogr. 39, 365–373.

Xue, K., Zhang, Y., Duan, H., Ma, R., Loiselle, S., Zhang, M., 2015. A remote sensing approach to estimate vertical profile classes of phytoplankton in a eutrophic lake. Remote Sens. 7, 14403–14427.

Yue, Y., Ni, J., Ciais, P., Piao, S., Wang, T., Huang, M., Borthwick, A.G., Li, T., Wang, Y., Chappell, A., Van Oost, K., 2016. Lateral transport of soil carbon and land-atmosphere CO2 flux induced by water erosion in China. Proc. Natl. Acad. Sci. U. S. A. 113, 6617–6622.

Zhang, Y., Qin, B., Zhu, G., Gao, G., Luo, L., Chen, W., 2006. Effect of sediment resuspension on underwater light field in shallow lakes in the middle and lower reaches of the Yangtze River: a case study in Longgan Lake and Taihu Lake. Sci. China Ser. D 49, 114–125.

Zhang, G., Yao, T., Chen, W., Zheng, G., Shum, C.K., Yang, K., Piao, S., Sheng, Y., Yi, S., Li, J., O'Reilly, C.M., Qi, S., Shen, S.S.P., Zhang, H., Jia, Y., 2019. Regional differences of lake evolution across China during 1960s–2015 and its natural and anthropogenic causes. Remote Sens. Environ. 221, 386–404.

Zhou, Y., Ma, J., Zhang, Y., Qin, B., Jeppesen, E., Shi, K., Brookes, J.D., Spencer, R.G.M., Zhu, G., Gao, G., 2017. Improving water quality in China: environmental investment pays dividends. Water Res. 118, 152–159.

Table 1. Statistical information about the in-situ SDDs collected in 299 Chinese lakes during 2003-2018. For sampling locations, please refer to Fig. 1. “std” denotes the standard deviation.

No.	Lake zones	Sampling year	Sampled lakes	Samples	*In-situ* SDD (cm)	
					Range	Mean ± std
1	IMXL	2008 – 2010, 2015, 2018	24	148	1.3–1117	126.4 ± 169.46
2	TPL	2008, 2012–2018	52	110	10–1650	557.42 ± 410.38
3	YGPL	2003, 2007, 2008, 2010, 2015	22	126	14–1390	261.08 ± 300.4
4	NPML	2008–2010, 2015–2018	62	285	3–690	75.37 ± 107.33
5	EPL	2007–2009, 2012, 2016–2018	139	1567	5–745	51.85 ± 46.63
In total		/	299	2236	1.3–1650	96.47 ± 178.27

Table 2 Mean contributions of different impact factors to annual changes of SDD. For each lake, the contributions were calculated by applying the multiple GLM analysis on annual mean data during 2000-2018. Numbers in the brackets denote how many lakes show significant SSD changes and are included in the statistics. Symbol "↑" denotes increase and "↓ "indicates decrease.

Lake zone	Change type	Wind (%)	Temperature (%)	Precipitation (%)	NDVI (%)	Others (%)
IMXL	Sig.↑(16)	13.55	18.05	10.71	44.95	12.74
	Sig.↓(2)	68.96	3.95	4.59	12.11	10.39
TPL	Sig.↑(126)	10.7	24.98	13.05	37.87	13.41
	Sig.↓(32)	16.77	19.41	17.9	29.62	16.29
YGPL	Sig.↑(3)	17.61	1.68	2.04	75.66	3.02
	Sig.↓(0)	/	/	/	/	/
NPML	Sig.↑(4)	6.24	6.19	12.64	58.12	16.81
	Sig.↓(2)	21.8	3.38	21.88	24.5	28.43
EPL	Sig.↑(27)	6.54	16.62	27.81	36.34	12.69
	Sig.↓(7)	12.86	23.65	22.46	30.45	10.58

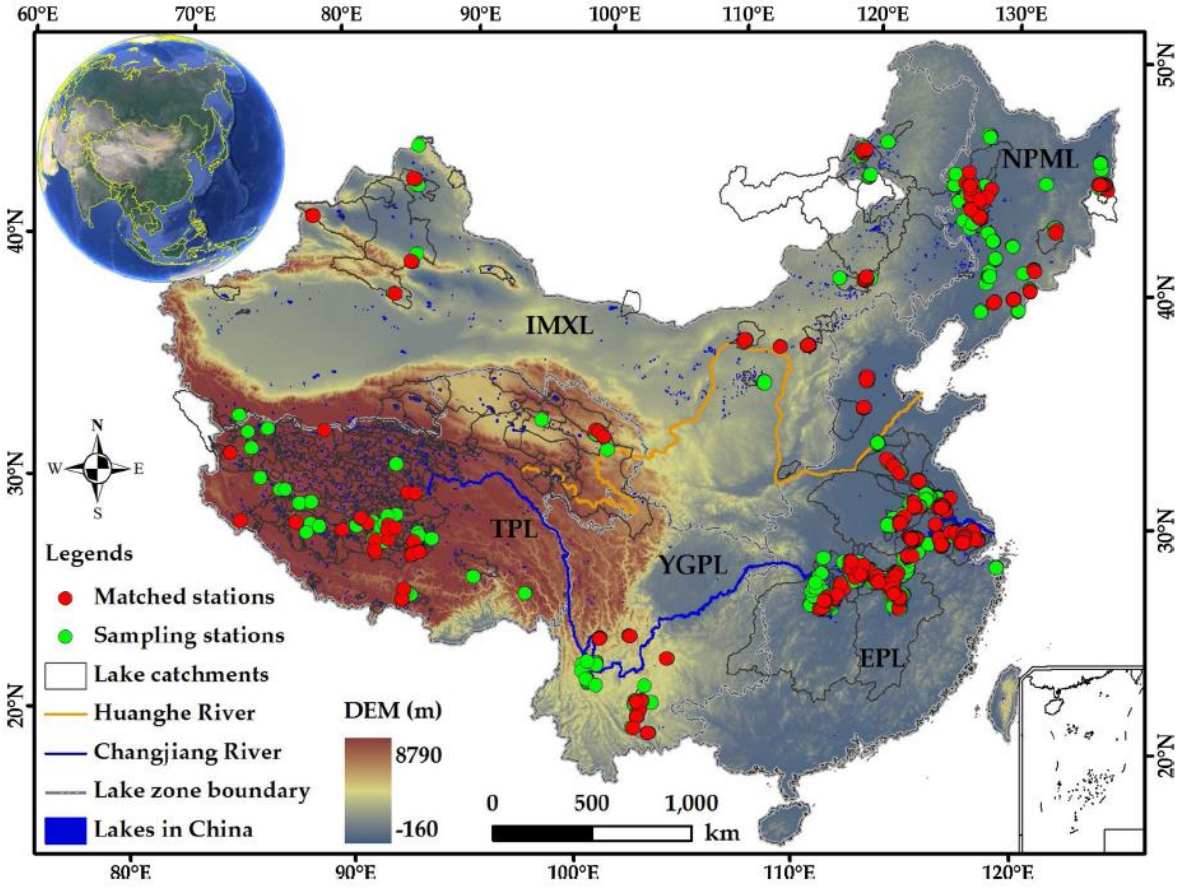

Fig. 1. The studied Chinese lakes and sampling stations. Only studied lakes with an area larger than 20 km2 are shown (N=412). All lakes are located within the five geographical zones: IMXL, TPL, YGPL, NPML, or EPL. The inset global map is sourced from Google Earth.

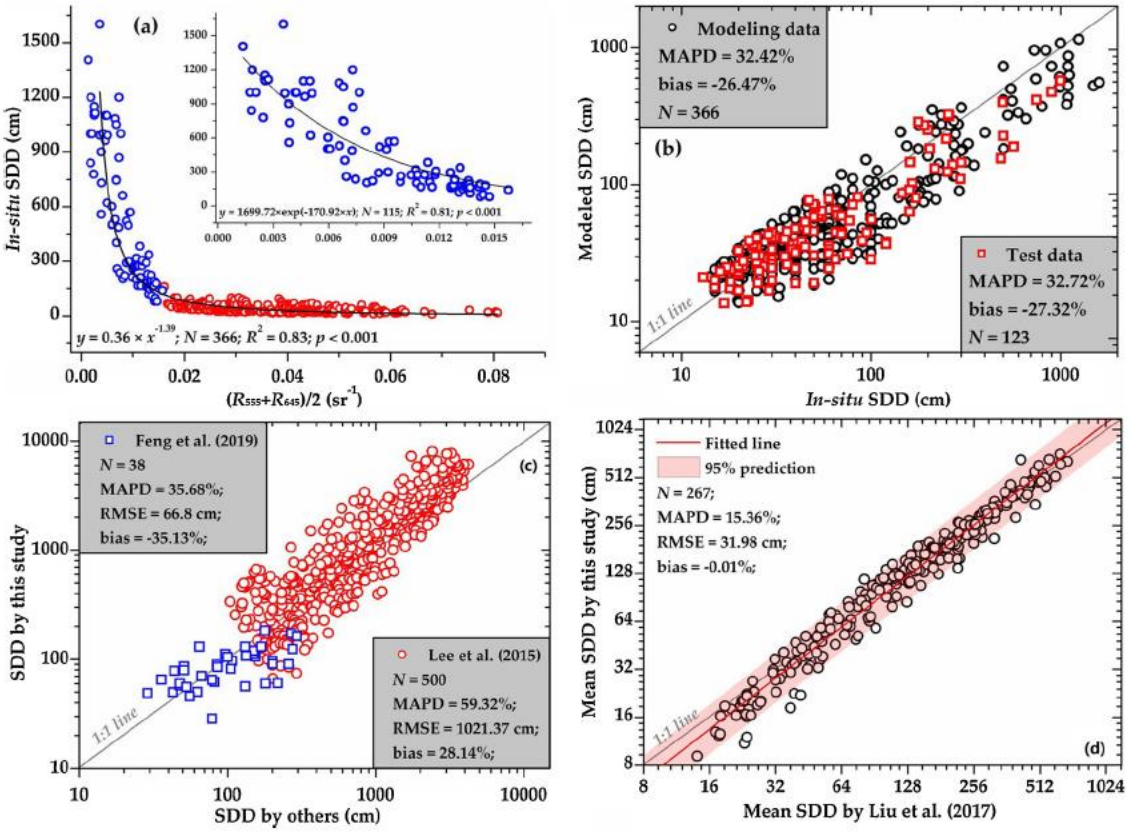

Fig. 2. The developed remote sensing algorithm for retrieving SDD and validation results. (a) The relationship between in-situ SDD and matched remote sensing reflectance of MOD09GA. (b) Comparisons between the satellite-derived and in-situ SDDs. (c) Comparisons between the modeled SDDs by this study and those by Feng et al. (2019) for lakes in the EPL and by Lee et al. (2015) for the synthesized dataset published by the International Ocean-Colour Coordinating Group (IOCCG, http://www.ioccg.org/). (d) Comparisons between the modeled SDDs by this study and those by Liu et al. (2017) for lakes in the TPL.

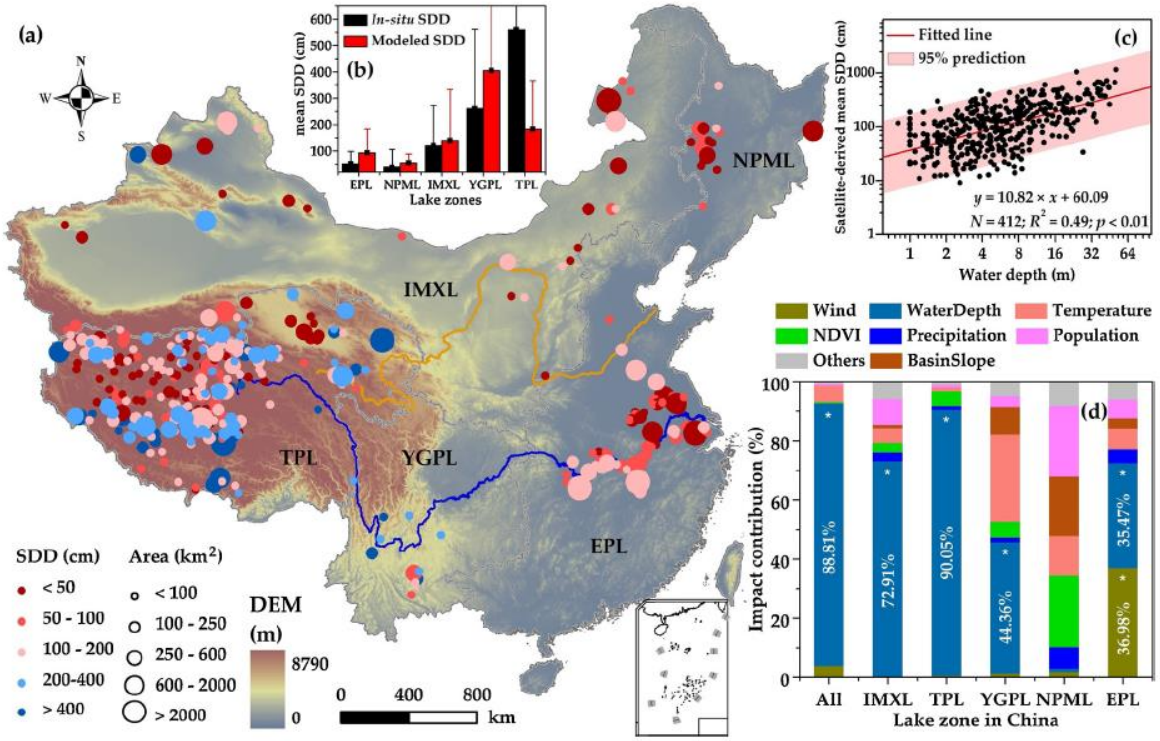

Fig. 3. Spatial pattern of SDD. (a) Satellite-derived climatological SDD during 2000-2018. According to the geographical features, five lake zones were defined: IMXL, TPL, YGPL, NPML, and EPL (Ma et al., 2010). Note that only ice-free results during May-September were used for the IMXL, TPL, and NPML (Cai et al., 2019). (b) Comparisons between in-situ and satellite-derived SDDs. (c) The linear relationship between SDD and lake water depth. (d) Impact contributions of different factors on the spatial distribution of SDDs in Chinese lakes. For all/regional lakes, the multiple GLM was applied on the climatological mean values of different lakes during 2000-2018 to quantify the contributions. Symbol "*" denotes $p < 0.05$.

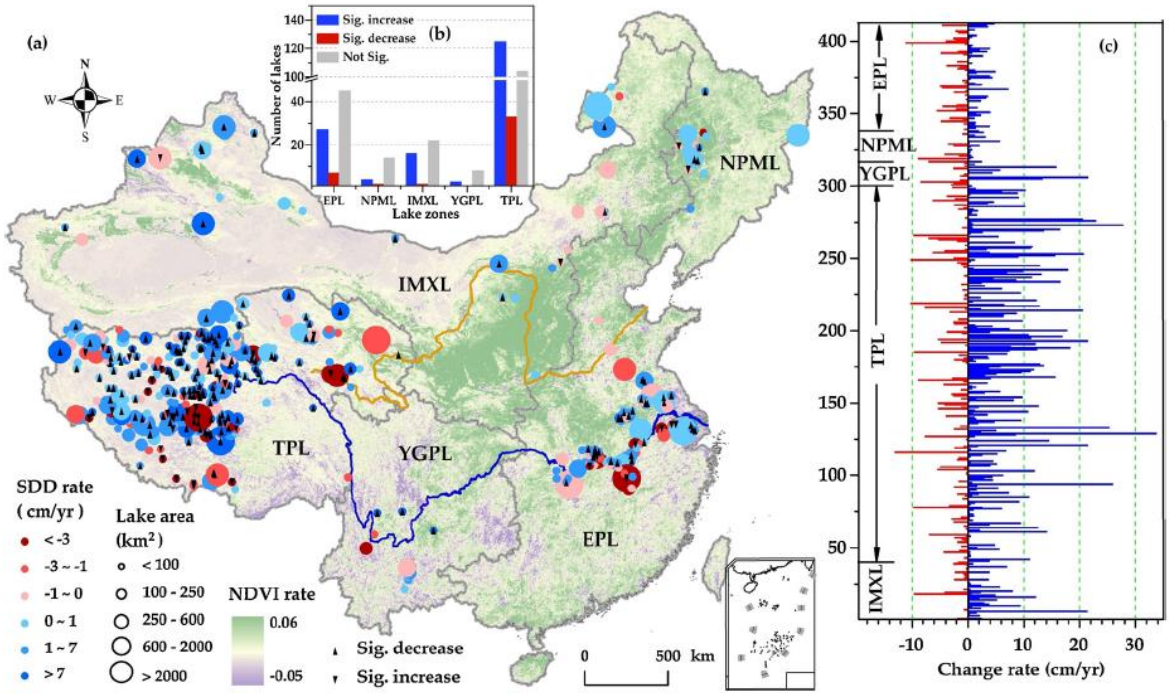

Fig. 4. Annual variations of SDD during 2000-2018. (a) Change rate of annual mean SDD. (b) Statistic results of different change types. (c) Change rates for all the 412 studied lakes. Lakes in each zone are numbered by increasing longitude.

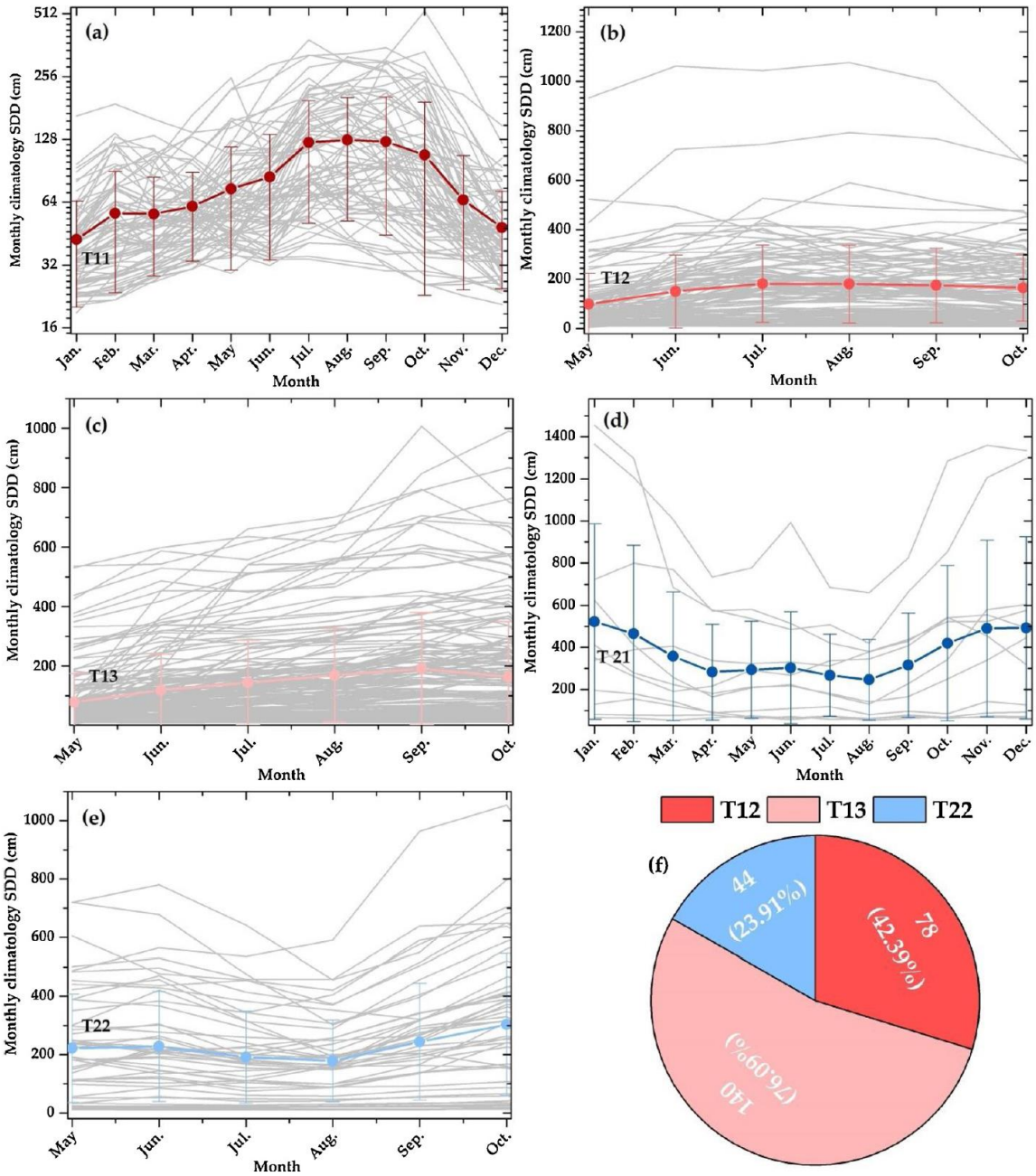

Fig. 5. Seasonal change types following one of the five prototypical pathways. (a) T11, (b) T12, (c) T13, (d) T21, and (e) T22 (Fig. 6). Grey lines show monthly climatological SDDs for different lakes, with colored symbols and lines showing pathway averages across lakes. (f) Statistic results of different types for the TPL zone.

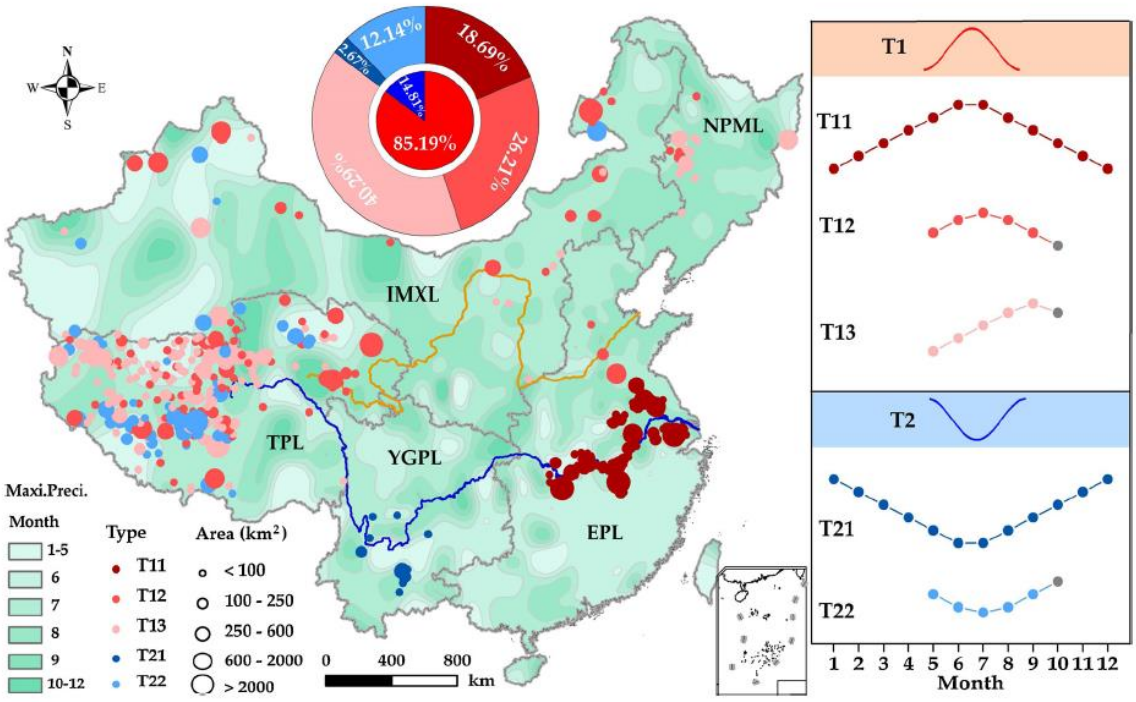

Fig. 6. Seasonal SDD types for Chinese lakes. Detailed classification results are shown in Fig. 5. For the three west lake zones, only ice-free data during May-September were used. However, to illustrate the seasonal cycle, we labeled SDD in October to the right concept map.

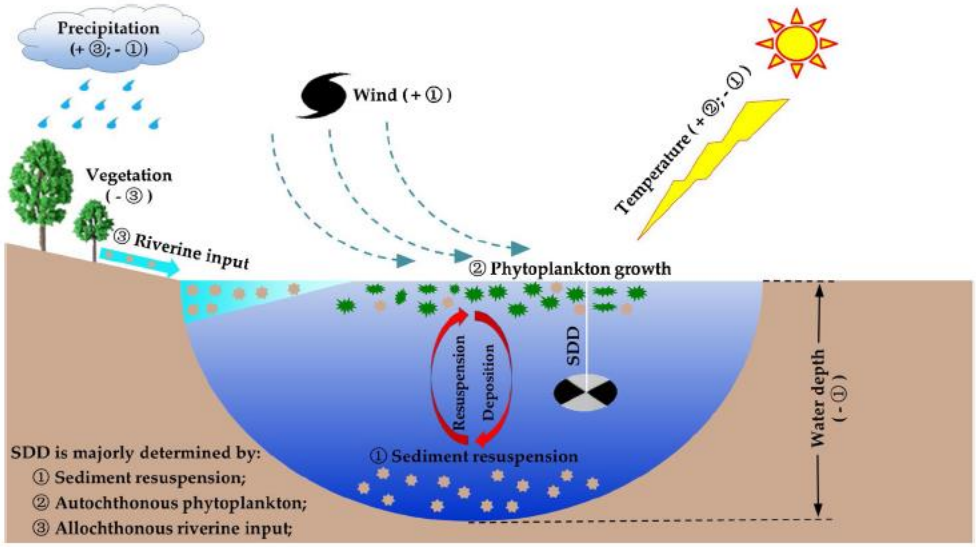

Fig. 7. Conceptual model showing the mechanisms responsible for the effects of different impact factors on SDD. ①, ②, and ③ are three TSM sources. Symbols "+" and "-" denote the increasing and decreasing effects, respectively.